Perturbative transfer matrix method for optical-pump terahertz-probe spectroscopy of ultrafast dynamics in spintronic terahertz emitters

Yingshu Yang ⬤, Stefano Dal Forno, and Marco Battiato[*]

School of Physical and Mathematical Sciences, Nanyang Technological University, Singapore 637371, Singapore

The rise of spintronic terahertz (THz) emitters has captured considerable attention owing to their potential for delivering high-intensity broadband THz pulses. The quest for enhancing their performance has largely concentrated on two key aspects: the out-coupling of THz radiation and its generation within the material system. A thorough understanding of THz generation and its interaction with photoexcited, out-of-equilibrium materials is pivotal for achieving further progress. Ultrafast optical excitations elicit a range of dynamic responses within the picosecond timescale, aligning with the THz frequency range. Although existing methodologies, such as optical-pump THz-probe experiments, offer valuable insights, the intricate details of spin current generation in spintronic THz emitters, including the possible delay between energy rise and spin current generation, continue to be somewhat obscure. To address this gap, we theoretically propose two approaches to extract the subpicosecond timescales involved in the complex process of converting a laser excitation to a THz pulse in spintronics THz emitter use. In doing so we leverage the interference of the THz-probe pulse interacting with time-varying material properties and the THz pulse generated by the spin-to-charge conversion process. To describe such processes and theoretically support the experimental approaches we suggest, we introduce the perturbative transfer matrix method to take into account both the interaction of a THz probe with a multilayer undergoing subpicosecond dynamics and the production of THz radiation within some of the layers.

I. INTRODUCTION

Spintronic terahertz emitters (STEs) have emerged as a subject of intense research focus due to their potential for high-speed applications [1,2]. STEs harness the phenomenon of ultrafast spin-to-charge conversion in magnetic/heavy metal multilayers to generate THz radiation, where a transient spin current, induced by optical excitation in a ferromagnet, is transformed into a charge current in the heavy metal, emitting a THz pulse [1,3,4]. Efforts to enhance the performance of these emitters have primarily centered on optimizing attributes such as bandwidth and amplitude. While the amplitude of THz pulses can be manipulated through material choice and varying pump amplitudes [5–9], understanding and controlling the bandwidth of the THz generated from STE, which largely depends on spin current generation dynamics, remains challenging [10].

Spintronic terahertz emitters have been analyzed using different techniques [11]. However, determining the time delays between optical excitation and spin current generation solely from the emitted signal has posed a significant challenge. Existing analyses have attempted to estimate these delays by comparing them with shift current generation, albeit yielding rough estimations due to the unclear timeframe in which the latter is also generated postpump [10].

To investigate how materials change post-photoexcitation, one common approach is to utilize optical-pump terahertz-probe (OPTP) and time-resolved terahertz spectroscopy (TRTS) analyses [12–14]. In OPTP experiments, the optical pump drives the system into an out-of-equilibrium state. Subsequently, a THz probe is sent onto the sample with variable delays to investigate its properties. The out-of-equilibrium dynamics can be used to access specific information like hot carrier lifetime [15,16], mobility [15,17,18], carrier density [19,20], relaxation and decay mechanism [20,21], as well as photoconductivity [15], which has to be deeply understood for the design and optimization of new-material-based devices [22]. The application of the OPTP experimental technique provides an in-depth analysis of these processes as well as information on the nonequilibrium status of materials such as semiconductors, superconductors, and metals, and other interesting materials such as Mxenes [23], perovskites [24], MoS_2 [25], graphene [13,26,27], and topological insulators [28], which are all important component to computers, lasers, light-emitting devices, electrodes, information storage devices, and future electronic devices [12,29–33].

To comprehend the time delays associated with the spin current generation, two primary challenges must be addressed: firstly, the timescales for both spin current generation and material heating are on the order of, at most, around 100 fs, far shorter than the duration of a standard THz-probe pulse. This situation renders analyses that assumes a quasistatic regime ineffective [34–40]. Secondly, the OPTP signals from a spintronic terahertz emitter encompass both THz-probe propagation and THz emission, thereby adding complexity to the interpretation of data.

*marco.battiato@ntu.edu.sg

Addressing the first challenge, the exploration of ultrafast dynamics using terahertz (THz) pulses has prompted the development of various methodologies aimed at elucidating OPTP experiments [41–47]. Notable pioneering efforts [42–45] have established a comprehensive frequency-domain methodology that enables the interpretation of material properties undergoing subpicosecond changes. These studies have laid the groundwork for understanding the interactions between THz pulses and photoexcited materials and have delved into the application of transfer matrix formalism for multilayer structures [48]. Furthermore, electromagnetic numerical time-domain simulations have been spotlighted for their potential [49–51], and substantial progress has been made in the development of time-domain formalisms [46,47].

Despite providing insightful solutions to the initial problem, these studies have primarily concentrated on the OPTP analysis of materials that do not emit THz radiation, leaving the secondary issue unaddressed. Although various theoretical and numerical techniques have been developed to individually model THz propagation in distinct scenarios [48,52,53], a unified framework that can simultaneously capture the interactions between optically excited multilayers and both the THz-probe and emission pulses has not yet been provided.

This paper aims to bridge the existing gap by introducing the perturbative transfer matrix method (PTMM). This approach is designed to simultaneously capture subpicosecond dynamics and comprehensively describe both THz-probe and emission processes. The PTMM model bears similarities to alternative models [41–48] for subpicosecond timescale analysis, yet it proves to be especially advantageous when investigating an STE within OPTP experiments, as illustrated in Fig. 1.

The PTMM model uniquely combines Drude dynamics and currents, crucial for THz pulse emission in spintronic devices. We put forth a holistic approach that illuminates both the propagation and generation of THz radiation in optically excited multilayers. The PTMM leverages a perturbation expansion of the Maxwell-Drude system, contrasted with equilibrium states, to reveal nuanced information in OPTP delay-resolved spectral maps. Additionally, we present a simple technique to decode the excitation time line. Our approach aligns cohesively with the transfer matrix method with source [53], enabling the assessment of the influence of spintronic THz emitters on OPTP signals. When an intrinsically emitted, optically triggered THz pulse intersects with a THz-probe pulse, we showcase the feasibility of using delay-resolved THz spectral maps to discern unique aspects of the ultrafast spin-to-charge conversion phenomenon.

This theoretical treatment allows us to propose two experimental approaches to extract subperiod timescale information on the microscopic processes leading to the emission of THz radiation from STE. First we show how a spectral analysis of the high-frequency tail of the OPTP spectrum (at the delay which makes the spectrum the broadest) can be used to get a sufficiently accurate estimation of the subpicosecond excitation timescale. Second, we show how the interference pattern between the THz probe and the emitted THz in STE gives reliable information on any delay between the optical excitation of the sample and the production of spin currents and, consequently, THz radiation.
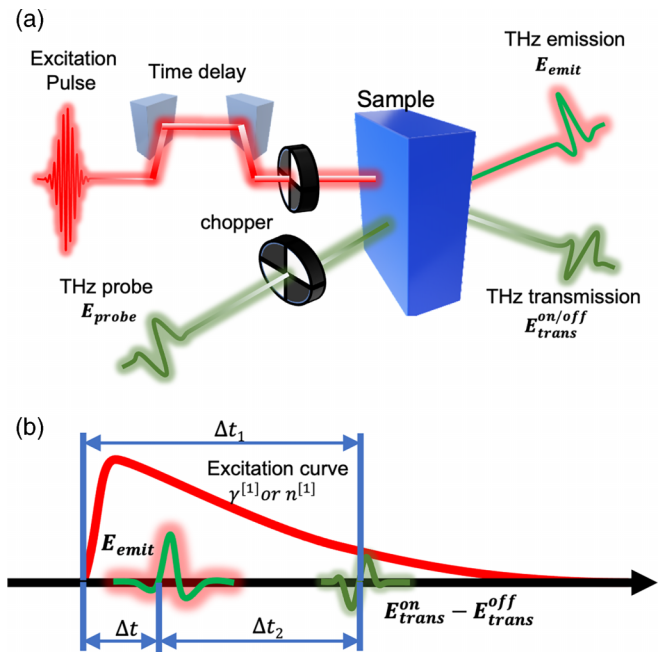

FIG. 1. Concept figure: a description of the OPTP and STE recipe. (a) A THz-probe pulse is sent into the system. The transmitted THz probe through an excited (pump-on, $E_{\text{trans}}^{\text{on}}$) and nonexcited (pump-off, $E_{\text{trans}}^{\text{off}}$) are measured. A THz emission pulse (E_{emit}) can also be measured when the sample is a spintronic THz emitter. (b) A theoretical layout of the time delays can be accessed using our recipe.

II. THEORETICAL BACKGROUND

Before addressing the proposed experimental approaches and describing what information can be extracted from them, we introduce the general theoretical framework that will be used to describe them. The transfer matrix method (TMM) is a well-established approach to describe the propagation of electromagnetic waves through multilayered systems, offering precise results by consolidating all left- and right-propagating waves into a single matrix [52]. A recent extension of this method, the transfer matrix with source (TMMS) [53], incorporates a spatially and temporally dependent source term that can be seamlessly integrated into the foundational TMM. That has been used to describe the production and extraction of THz radiation within STEs.

However, the complexity increases in OPTP experiments, where an optical-pump pulse precedes the THz probe into the multilayer system, causing the optically excited sample to undergo rapid changes in its dielectric responses, followed by a slower relaxation back to equilibrium. For an OPTP of a spintronic terahertz emitter, the situation is further complicated by the concurrent occurrence of THz transmission through both equilibrium and photoexcited out-of-equilibrium systems, along with THz emission within the system.

To fully describe these effects, several steps are necessary. Assuming the optical excitation occurs in the linear regime and that saturation processes in absorption are negligible, the distribution of optical photon energy within the material can be determined using the standard TMM [49,52,54] at optical frequencies. Knowing the spatial distribution of the optical excitations is important to be able to compute the

time evolution of the sample's out-of-equilibrium state—the time dependence of the material properties as well as the spatial and temporal profile of any spin and charge current. In this work we do not address this step and we assume those dynamics to be known (or, as we will see later, to be extracted by comparison with experiments). We focus here on the next step, since even when the time and position dependence of the material properties and the currents is known, the description of the propagation of a THz probe is more complicated and using the TMM will not suffice.

First of all, let us remember that the aim of the OPTP technique is to measure the difference between the THz transmission through the sample at equilibrium and the one out-of-equilibrium. Solving the TMM for the THz probe with equilibrium properties (similar to what is done to compute the position-resolved absorption of the optical pulse) will only provide the pump-off THz transmission. To obtain the pump-on signal, we undertake a perturbation expansion of the Maxwell-Drude system. For this expansion we will assume that the frequency-dependent total permittivity $\epsilon_T[\omega]$ of the material can be written as the sum of a Drude component $\epsilon_D[\omega]$ and a remaining background component $\epsilon_B[\omega]$, which accounts for all the non-Drude contributions (e.g., the interband transitions) with a generic frequency dependence. We further assume that the background component of the permittivity is not modified by the laser. Conversely, we will allow the Drude parameters to be explicitly time dependent. Here we specifically consider the scattering rate γ and carrier density n. We write the Drude parameters as the sum of their equilibrium values, $\gamma^{[0]}$ and $n^{[0]}$, and a time-dependent part, $\gamma^{[1]}[t]$ and $n^{[1]}[t]$. We assume that such time dependence is either known or is to be fitted to experimental results using the treatment that we will develop in the present work.

Upon expanding the Maxwell-Drude system, we discern that the entire system can be partitioned into zeroth-order and first-order equations. The zeroth-order equations align with the standard Maxwell equations and can be readily solved using the TMM. The first-order equations resemble the Maxwell-Drude system but with an additional source term (which has the dimensionality of a volume current) that contains a combination of the changes to the dielectric response and the zeroth-order fields. The first-order equations can be solved using the TMMS method developed in Ref. [53]. By integrating the Maxwell-Drude expansion with the TMMS solutions, we formulate the perturbative transfer matrix method. A comprehensive overview of this approach is provided in Appendixes A and B.

To analyze the propagation of electromagnetic radiation through a multilayered heterostructure at normal incidence, we employ the following notation: layers are enumerated from left to right using an index n, which starts at 1 and extends to the total number of layers N. The multilayered system is assumed to be enclosed by air, with the air on the left (right) assigned an index of 0 ($N + 1$) and considered semi-infinite. The thickness of each layer is represented by d_n. Furthermore, we assume that no 2D currents form between the layers (all currents are considered volume currents), ensuring the continuity of the electric and magnetic fields across the interfaces.

Given this system and notation, along with the final expressions derived from the PTMM, we can demonstrate that the

TABLE I. The theoretical expression and the experimental labeling.

Equation terms	Experimental labels
$f_0^{[0]>} * t_a$	$E_{\text{trans}}^{\text{off}}$
$J_{\text{emit}}^> - t_b J_{\text{emit}}^<$	E_{emit}
$J_{\text{perb}}^> - t_b J_{\text{perb}}^<$	$E_{\text{trans}}^{\text{on}} - E_{\text{trans}}^{\text{off}} = \Delta E$

overall THz transmission results, up to the first perturbative order, can be succinctly expressed as

$$f_{N+1}^> = f_0^{[0]>} t_a + (J_{\text{emit}}^> - t_b J_{\text{emit}}^<) + (J_{\text{pert.}}^> - t_b J_{\text{pert.}}^<). \quad (1)$$

Here $f_{N+1}^>$ denotes the right-propagating wave amplitude in the right semi-infinite layer, $f_0^{[0]>}$ represents the input THz-probe wave amplitude from the left semi-infinite layer, $J_{\text{emit}}^<$ and $J_{\text{emit}}^>$ correspond to the left- and right-propagating waves generated in the excited layer from the STE, and $J_{\text{pert.}}^<$ and $J_{\text{pert.}}^>$ represent the left- and right-propagating waves in the excited layer from the OPTP corrections. The coefficients t_a and t_b represent the transmission coefficient of the entire system and a specific coefficient expressible using elements of the overall transfer matrix, respectively. A detailed derivation and expression of these terms can be found in Appendixes A and B.

Therefore, in summary, the first term in Eq. (1) refers to the THz transmission through the unperturbed sample (the transmission of the THz probe with pump off, $E_{\text{trans}}^{\text{off}}$), which can be used to describe the THz-TDS (time-domain spectroscopy) results. The second term refers to the THz emission from a sample where one layer carries a charge current that produces THz (E_{emit}), which can be used to describe the STE results. (Notice that further THz-producing layers can be straightforwardly added as further terms in the summation.) Finally, the third term refers to the correction of the transmission when the pump is on (the transmission difference of the THz probe through a sample with the pump on and pump off, $E_{\text{trans}}^{\text{on}} - E_{\text{trans}}^{\text{off}} = \Delta E$). A summary of the relationships between the equation and the experiment labels is reported in Table I.

III. RESULTS

To show the capabilities of the PTMM, we apply the approach to two test cases. Firstly, we show how a THz probe traverses a laser-excited sample. We choose a quartz(1 mm)/Fe(3 nm)/Pt(3 nm) heterostructure as an example (of course, the proposed approach can be applied to any stack of materials). Although the chosen heterostructure is a commonly used spintronics THz emitter, in the first test case we initially ignore the THz that is produced within the sample. The produced THz will be then be explicitly treated and its interference with the THz-probe pulse accounted for in the second test case.

We set the dielectric response of quartz at equilibrium by using a real frequency-independent refractive index of 2.01 [55,56] (yet notice that the model works for any generic frequency-dependent response). Also, we model the dielectric response of the metallic layers using the Drude model and

set the plasma and damping frequency to 4.091 and 0.018 eV for Fe, and 5.145 and 0.069 eV for Pt, respectively [57]. No further contributions to the response of Fe and Pt at equilibrium have been considered (yet a further contribution to the dielectric function with a generic frequency dependence can be included). In addition, for simplicity we considered only the excitation of the Pt layer. The excitation of the Fe layer will simply add another term to Eq. (1) and can be simply written as

$$f_{N+1}^> = f_0^{[0]>} t_a + (J_{\text{emit}}^> - t_b J_{\text{emit}}^<)$$
$$+ (J_{pert.Pt}^> - t_b J_{pert.Pt}^<)$$
$$+ (J_{pert.Fe}^> - t_b J_{pert.Fe}^<). \quad (2)$$

If the excitation and de-excitation timescales for both Pt and Fe are similar, their contributions to the THz response will simply sum up in phase. Interesting effects can happen if the dynamics of Fe and Pt do not happen on the same timescales; however, such a study goes beyond the scope of the present work.

In the following example we will explicitly address only the case of $\gamma^{[1]} \neq 0$ and $n^{[1]} = 0$. We also neglect any effect of the optical laser excitation on quartz. Finally, we assume that Pt experiences an increase $\gamma^{[1]}[t]$ in its Drude scattering rate in the form

$$\gamma^{[1]}[t] = h \frac{e^{-\frac{t-t_0}{\tau_{\text{decay}}}}}{e^{-\frac{(t-t_0)-\tau_{\text{rise}}/2}{\tau_{\text{rise}}/4}} + 1}, \quad (3)$$

where h controls the maximum scattering rate change, τ_{rise} is the increase time and τ_{decay} is the following decrease time, and t_0 is the time position of the excitation. We stress that the focus of this work is to describe the propagation of THz waves through an optically excited system. Equation (3) is meant purely as an example, mimicking common excitation and thermalization dynamics. However, as already mentioned earlier, a proper form for $\gamma^{[1]}$ and $n^{[1]}$ should be obtained with other methods in future analysis. In addition, a theoretically built THz-probe pulse with a central frequency (f_c) of 1.5 THz is used in the following calculations.

A. The subpicosecond excitation timescale

In this section we will demonstrate that the time-resolved spectra obtained by OPTP experiments contain enough information to evaluate the timescale of the fast excitation after the laser pump, even when it is much shorter than the probe pulse time-width. We note that although we are nominally using a Fe/Pt heterostructure as an example, we will not be describing the emission at this stage. Therefore the results below apply to any femtosecond-laser-excited heterostructure probed by THz pulses.

We assume the temporal shape of $\gamma^{[1]}[t]$ known and vary the pump-probe time delay. Figure 2(a) shows the respective time positions of the pump and probe pulses, where the time axis is centered around the THz-probe pulse, and the time dependence of the change in the scattering rate $\gamma^{[1]}[t]$ is shifted in time to simulate the experimental variable delay time. Figures 2(b)–2(e) show the time-resolved THz-probe transmission differential spectra (pump-on minus pump-off)
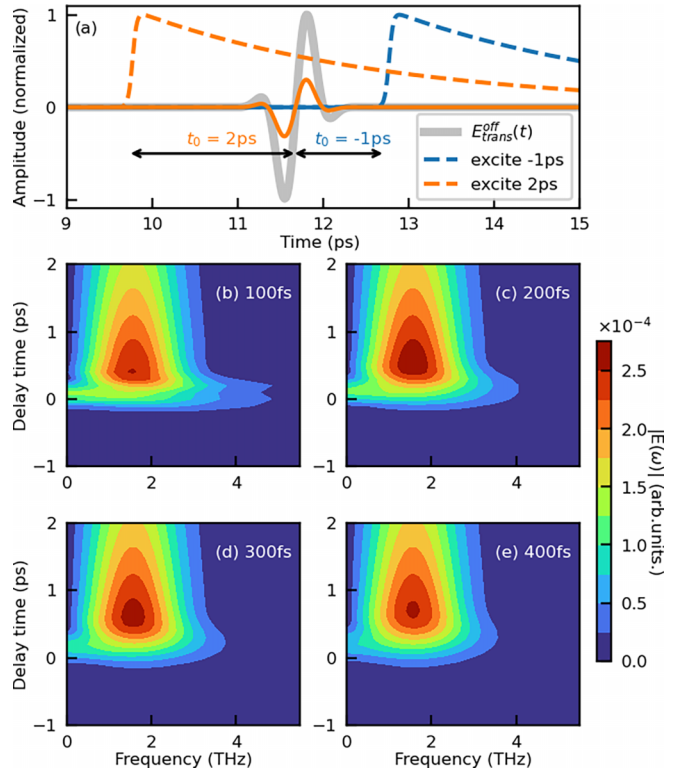

FIG. 2. (a) Shows the excitation curve $\gamma^{[1]}$ at different initial time delays and its corresponding frirst-order correction term $E_{\text{trans}}^{\text{on}} - E_{\text{trans}}^{\text{off}}$ change. (Note that the profiles are normalized and not in scale, showing only a comparison in the shapes). (b)–(e) Frequency maps of $|E_{\text{trans}}^{\text{on}} - E_{\text{trans}}^{\text{off}}|$ at different increase times ($\tau_{\text{rise}} = 100, 200, 300,$ and 400 fs) as a function of frequency and time delay change.

for four different τ_{rise} times (τ_{decay} has been kept the same for all four cases).

At sufficiently large negative delay times in Figs. 2(b)–2(e), the probe pulse arrives well before the laser excitation [dashed blue line in Fig. 2(a)]. The transmitted THz probe is not altered: the difference between the transmitted probe with the pump on and - off [full blue line in Fig. 2(a)] is zero. On the other hand, when the probe pulse arrives well after the sharp excitation dynamics right after the laser excitation [dashed orange line in Fig. 2(a)], the transmitted THz probe is altered [full orange line in Fig. 2(a)] mostly in amplitude, while its temporal shape, and therefore the spectrum, is not altered. This is evident from Figs. 2(b)–2(e), where the time-resolved spectra for sufficiently large positive delays simply decrease in amplitude. The time evolution of the differential transmission gives a clear indication of the de-excitation dynamics of the sample τ_{decay}. On the other hand, the spectrum of the differential transmission does not contain any interesting information, since it mostly reproduces the probe-pump spectrum. This happens because the change in $\gamma^{[1]}[t]$ is relatively slow and a quasistatic description of the THz propagation could be adopted.

Conversely, the situation is very different when the delay is such that the probe pulse overlaps with the fast rise dynamics in the excitation [small delays in Figs. 2(b)–2(e)]. Here we notice two important features. The timescale over which

the differential spectrum shows an overlap between the fast timescale $\tau_{\rm rise}$ and the probe pulse is rather independent of the rise time $\tau_{\rm rise}$ itself. This is indeed because the overlap time is mostly controlled by the THz pulse time-width. For this reason, the temporal duration of this feature does not give any insight into the time evolution of the material's dielectric properties. What is instead evident is that the spectrum during the overlap is strongly affected by the $\tau_{\rm rise}$ time [see Figs. 2(b)–2(e)].

The analysis of the spectrum map reveals two interesting findings. Firstly, it is observed that the spectrum is the broadest when the excitation overlaps with the central time position of the probe. Secondly, a faster increase time for the excitation profile results in a broader spectrum map. We find that it is possible to obtain a fairly accurate estimation of the fast rise time $\tau_{\rm rise}$. This can be achieved by selecting the delay time at which the spectrum is the widest. At that time delay one should identify the frequency $f_{1\%}$ at which the spectrum has 1% of its maximum amplitude. The fast rise time $\tau_{\rm rise}$ can then be estimated using

$$\tau_{\rm rise} \approx \frac{1}{f_{1\%} - 2f_c}, \tag{4}$$

where f_c is the central frequency of the THz probe.

To prove that the formula above provides a good estimation of the fast rise time $\tau_{\rm rise}$ even when it is much shorter than the THz-probe time-width, we fix the delay time between the probe and excitation at the point of overlap and compute the differential spectrum for varying rise times $\tau_{\rm rise}$ [as shown in Fig. 3(a), where the reader should notice the logarithmic intensity scale]. The blue line in the main figure of Fig. 3(b) represents simply the conversion of $\tau_{\rm rise}$ to frequency. It is already evident how the inverse rise time remains approximately parallel to the level lines. After some fine-tuning we find that the best estimation of $\tau_{\rm rise}$ is obtained by Eq. (4) where a correction including the central frequency of the probe has been added. The error that occurred when using the estimation above is shown in the inset in Fig. 3(b).

The above-mentioned correspondence, although very convenient due to its simplicity, is not perfect. For an accurate extraction of the excitation time, a comparison between experiments and theory is needed. It is, however, important to note how the method can clearly resolve timescales (hundreds of femtoseconds) that are shorter than the period and time-width of the employed radiation (≈ 2 ps in the presented example).

The analysis above can be conducted easily on any excited multilayer that does not produce THz upon laser excitation. It is however possible to perform the above analysis in heterostructures used for spintronics THz emitters. In this case the time-resolved spectra cannot be simply constructed by subtracting the THz-probe transmission with pump on by the THz-probe transmission without pump: the THz radiation internally generated by the sample must be subtracted as well. This can be achieved because the THz signal produced by the inverse-spin Hall effect (ISHE) is proportional to the optical-pump intensity but not to the THz probe, while the spectral maps in Fig. 2 are proportional to both the optical-pump intensity and the THz-probe amplitude.
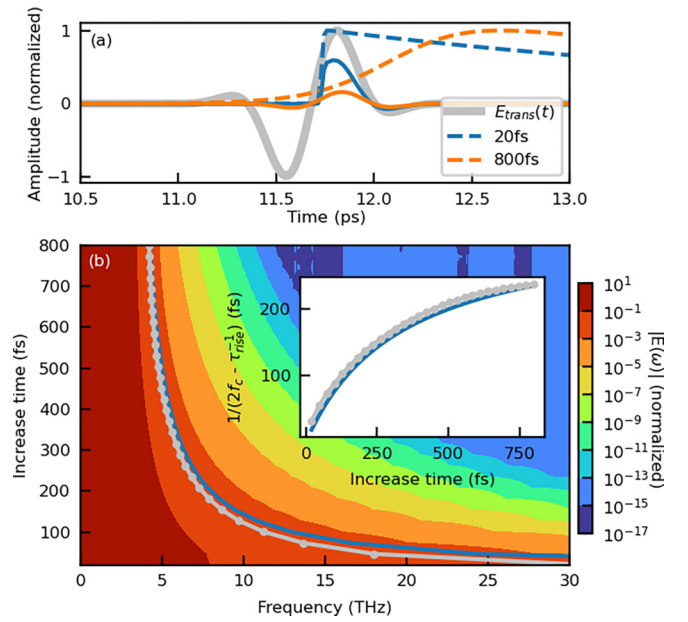

FIG. 3. (a) Shows the excitation curve $\gamma^{[1]}$ at a fixed time t_0 but with different increase time parameters $\tau_{\rm rise} = 20$ fs and $\tau_{\rm rise} = 800$ fs. (Note that the profiles are normalized and not in scale, showing only a comparison in the shapes). (b) Normalized frequency map of OPTP signal as a function of the frequency and increase time $\tau_{\rm rise}$. The pump-probe delay time is fixed at $t_0 = 0$ ps. The gray dotted line shows the region where the spectrum amplitude is 1% of its maximum ($f_{1\%}$). The blue line is $f_c * 2 + 1/\tau_{\rm rise}$. Inset: The inverse plotting of the extracted gray dotted line and blue line on the map.

B. Pump-THz emission time delay

We here focus completely on the analysis of spintronics THz emitters: these are (in their simplest configuration) a bilayer system with a ferromagnetic (FM) layer and a nonferromagnetic (HM) layer, where after excitation a spin current transfers from FM to HM, undergoes ISHE to become a charge current, and eventually emits terahertz radiation [1,2]. After determining the exact time when the excitation and the probe overlap in the system, we are now able to proceed to another type of spectrum analysis, which is when the THz emission and first-order correction (ΔE) exist at the same time, and their interference patterns can be analyzed to extract further information. As a reminder, the shape of the THz wave emitted from the STE differs from that of the THz-probe wave. The emitted THz shape is determined based on a characteristic spin current profile, exhibiting a trend of a rapid increase followed by a gradual decrease. For a comprehensive understanding of the emitted THz shape, please consult Ref. [53].

In this analysis we obtained an overall spectrum map of the changing time delay between the excitation and probe, only that now the THz emission has not been subtracted (as shown in Fig. 4). The THz emission will happen after a certain time [Δt shown in Fig. 1(b)] of the excitation, which is usually believed to be only tens of femtoseconds, specifically estimated as 120 fs in recent works [10]. Notice that the shape of this interference spectrum depends on the relative amplitude of the emitter THz and the first-order correction to the transmission
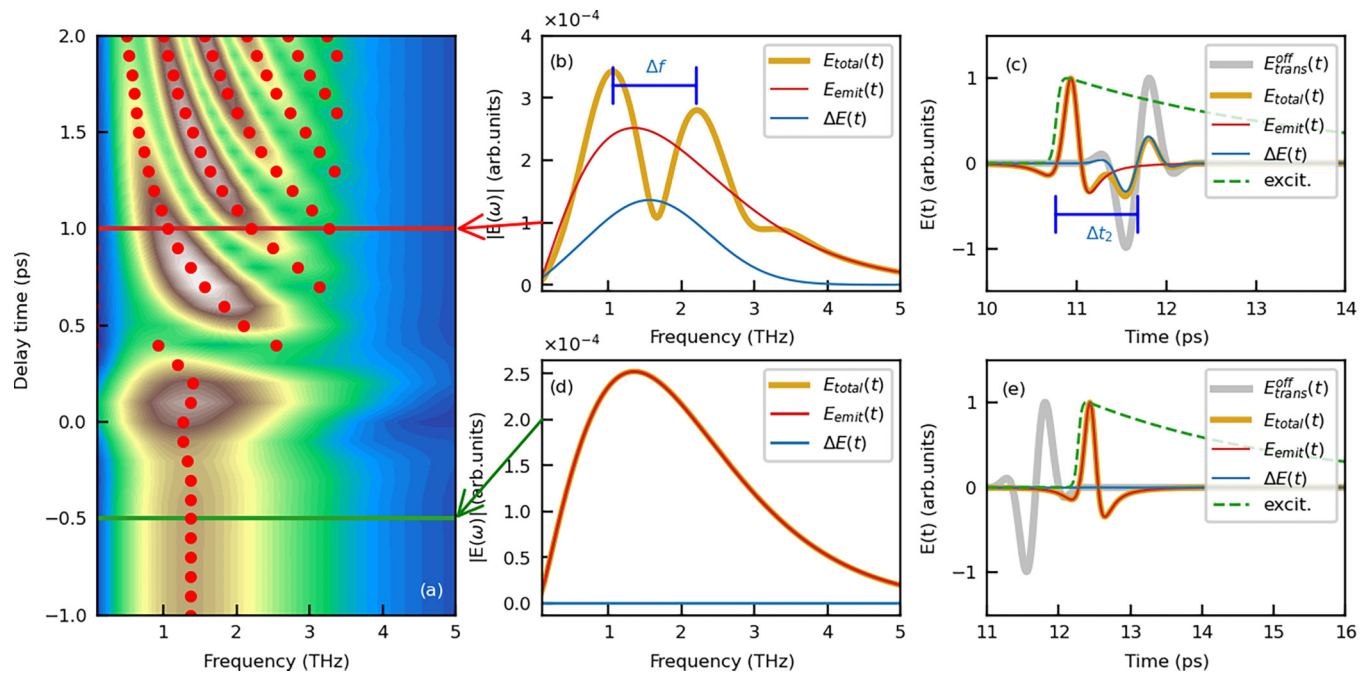
FIG. 4. Pump-probe analysis of Spintronic THz emitter. (a) An overall spectrum map ($E_{\text{emit}} + \Delta E$) as a function of frequency and delay time. The red dots on the map show the peaks of the spectrum at different time delays. (b, c) The spectrum and its corresponding THz profiles in the time domain for case 1 (probe sent in after the excitation). (d, e) The spectrum and its corresponding THz profiles in the time domain for case 2 (probe sent in before the excitation). Notice that the profiles in the time domain are normalized.

of the THz probe. Maximal interference (and therefore the easiest spectral map to analyze) is obtained when the two contributions have similar amplitudes. This can be obtained experimentally by varying the probe intensity.

In the spectrum map we observe that when we send the probe in after the excitation, more than one peak will exist in the overall spectrum [red dots in Fig. 4(a)]. We now focus on two specific cases: when the probe is sent in after the system is excited [Figs. 4(b) and 4(c)] and when the probe is sent in before the system is excited [Figs. 4(d) and 4(e)]. We find that the spectrum shows interference peaks for case 1, while for case 2 the overall spectrum is equal to the THz emission spectrum.

Interestingly, the frequency difference between the peaks (Δf) of the overall spectrum for case 1 is going to give us valuable information about the time difference between the emission pulse and the correction pulse [Δt_2 in Figs. 1 and 4(c)]. In fact, we see that

$$\Delta t_2 \approx \frac{1}{\Delta f}. \tag{5}$$

IV. CONCLUSIONS

In this study we have devised a comprehensive theoretical framework for analyzing the nuances of subpicosecond changes in optical-pump terahertz-probe (OPTP) experiments, with a focus on spintronic terahertz emitters (STEs). We have illustrated a cohesive approach to integrating THz transmission through systems at equilibrium and nonequilibrium states along with THz emission from STEs.

Our investigation has yielded critical insights into the temporal dynamics of ultrafast laser excitations as captured by

OPTP measurements. We have delineated a process to determine two essential time delays: the time delay between the probe and the excitation pulse (Δt_1), which can be inferred from the spectrum map of changing time delay, and the interval between THz emission and the probe pulse (Δt_2), which can be extrapolated from the comprehensive spectrum map of THz emission. Combining these metrics, we can obtain the time lag between THz emission and excitation ($\Delta t = \Delta t_1 - \Delta t_2$), a critical parameter for the optimization of STE bandwidth. While the estimation of Δt_2 can be done with relatively good resolution, obtaining a sufficiently precise Δt_1 is not easy using the method we suggest. In our future work we will explore techniques to obtain a more precise estimation of Δt_1, in particular, by performing a complete fitting of the OPTP time-resolved spectral map using PTMM. The findings from our theoretical exploration provide a nuanced understanding of rapid temporal dynamics in OPTP experiments, thereby enhancing the body of knowledge within the field of ultrafast laser excitations and contributing to the optimization of spintronic terahertz emitter technologies.

APPENDIX A: PERTURBATION EXPANSION OF THE MAXWELL-DRUDE SYSTEM

To commence, we consider the scenario of electromagnetic wave propagation in a homogenous medium undergoing temporal changes in material properties due to femtosecond

laser stimulation and the ensuing thermalization process. The comprehensive frequency-responsive permittivity, denoted by $\epsilon_T[\omega]$, is written as the aggregate of a Drude term $\epsilon_D[\omega]$ and a residual background term $\epsilon_B[\omega]$. This background term represents all non-Drude factors (such as interband transitions) with a characteristic frequency response. It is assumed that (and the treatment is limited to cases where) the laser excitation does not alter the background permittivity component. However, we do allow for the parameters defining the Drude component to vary with time.

In the above situation, the electric E and magnetic H fields propagating along the z axis are described by the Maxwell-Drude system:

$$\partial_z E[z, \omega] = -i\,\omega\,\mu[\omega]\,H[z, \omega],$$
$$\partial_z H[z, \omega] = -i\,\omega\,\epsilon_B[\omega]\,E[z, \omega] + J[z, \omega],$$
$$\partial_t J[z, t] = -\gamma J[z, t] + \frac{ne^2}{m}E[z, t], \tag{A1}$$

where μ is the permeability of the medium, $J[z, t]$ is the current density (along the same direction as the electric field) induced by the Drude response, e is the electron charge, m the effective mass, n is the number of carriers, and γ the inverse scattering lifetime.

In the case n and γ are constant in time, and the last equation leads to the known expression for the Drude conductivity:

$$\sigma_D[\omega] = \frac{ne^2}{m(\gamma - i\omega)}. \tag{A2}$$

The total permittivity $\epsilon_T[\omega]$ (i.e., the background contribution and the Drude contribution) then reads

$$\epsilon_T[\omega] = \epsilon_B[\omega] + i\frac{\sigma_D[\omega]}{\omega}. \tag{A3}$$

On the other hand, the case where the number of carriers n and the inverse scattering lifetime γ depend on time represents a material in- an out-of-equilibrium state. For example, an increase in the number of carriers may describe the transient photodoping of a semiconductor during a femtosecond laser excitation, while its decrease could be due to the subsequent carrier recombination. Similarly, a change in γ may describe the increased number of scatterings triggered by the increased phonon temperature after an excitation. We write the Drude parameters as the sum of their equilibrium values, $\gamma^{[0]}$ and $n^{[0]}$, and a time-dependent part, $\gamma^{[1]}$ and $n^{[1]}$:

$$\gamma[z, t] = \gamma^{[0]} + \gamma^{[1]}[z, t], \tag{A4}$$

$$n[z, t] = n^{[0]} + n^{[1]}[z, t]. \tag{A5}$$

Notice that we allow for the variations to also be position dependent.

If we assume that the time variations are small, we can write the fields and the current up to the first perturbative order as

$$E[z, t] \approx E^{[0]}[z, t] + E^{[1]}[z, t],$$
$$H[z, t] \approx H^{[0]}[z, t] + H^{[1]}[z, t],$$
$$J[z, t] \approx J^{[0]}[z, t] + J^{[1]}[z, t], \tag{A6}$$

where the two orders must satisfy two different sets of equations. Before proceeding let us stress here the crucial point of this approach: the perturbative expansion does not impose any requirement for the variations to be slow. This is critical, since we aim to address the case where the material properties are changing over a similar timescale as the THz radiation period.

The zeroth order satisfies the unperturbed Maxwell-Drude system in Eqs. (A1), with constant equilibrium Drude parameters, and reads

$$\partial_z E^{[0]}[z, \omega] = -i\omega\mu[\omega]H^{[0]}[z, \omega],$$
$$\partial_z H^{[0]}[z, \omega] = -i\omega\epsilon_T[\omega]E^{[0]}[z, \omega]. \tag{A7}$$

This set of equations can be solved analytically using a standard transfer matrix method approach [52], as we show in Sec. B 1.

The first-order set of equations will read

$$\partial_z E^{[1]}[z, \omega] = -i\omega\mu[\omega]H^{[1]}[z, \omega],$$
$$\partial_z H^{[1]}[z, \omega] = -i\omega\epsilon_B[\omega]E^{[1]}[z, \omega] + J^{[1]}[z, \omega],$$
$$\partial_t J^{[1]}[z, t] = -\gamma^{[0]}J^{[1]}[z, t] + \frac{n^{[0]}e^2}{m}E^{[1]}[z, t]$$
$$- \gamma^{[1]}[z, t]J^{[0]}[z, t] + \frac{n^{[1]}[z, t]e^2}{m}E^{[0]}[z, t]. \tag{A8}$$

Here $\gamma^{[0]}$, $\gamma^{[1]}$ $n^{[0]}$, $n^{[1]}$ should be provided as inputs in the following and are assumed to be obtained by other methods. Notice how the first-order set of equations satisfies a similar expression to the zeroth order and reads

$$\partial_z E^{[1]}[z, \omega] = -i\,\omega\,\mu[\omega]\,H^{[1]}[z, \omega],$$
$$\partial_z H^{[1]}[z, \omega] = -i\,\omega\,\epsilon_T[\omega]\,E^{[1]}[z, \omega] + \mathcal{J}[z, \omega], \tag{A9}$$

where the source term is given by

$$\mathcal{J}[z, \omega]$$
$$= \sigma_D^{[0]}[\omega]\mathcal{F}\left[\frac{n^{[1]}[z, t]}{n^{[0]}}E^{[0]}[z, t] - \frac{m\,\gamma^{[1]}[z, t]}{n^{[0]}\,e^2}J^{[0]}[z, t], \omega\right] \tag{A10}$$

and has the dimensionality of a volume current. For later convenience, we express the source in terms of its spatial Fourier transform:

$$\mathcal{J}[z, \omega] = \sum_l \mathcal{J}[k_l, \omega]\exp[i\,k_l\,z]. \tag{A11}$$

So far we have modeled the effect of time-varying Drude parameters on Maxwell's equations within a single layer. We have found that by expanding the electric and magnetic fields in orders of the time-dependent correction to the equilibrium Drude parameters, the zeroth order satisfies the standard Maxwell's equations, while the first order satisfies the nonhomogeneous equations (A9). In the following section we will see how to solve them for a system of layered materials and how to describe an OPTP experiment.

APPENDIX B: PERTURBATIVE TRANSFER MATRIX METHOD

To address the propagation of electromagnetic radiation through a multilayered heterostructure at normal incidence we use the following notation. We count layers from left to right using an index n starting from 1 up to the number of layers N. We assume the multilayered system to be sandwiched by air. The air on the left (right) has index 0 ($N+1$) and is assumed to be semi-infinite. The layer thickness is denoted by d_n. Also, we assume that no two-dimensional currents build up at the interface between layers so that the electric and magnetic fields across the interfaces are continuous.

1. Zeroth-order propagation

For the zeroth order, we follow the textbook TMM (a derivation with symbols consistent with this article can be found in Ref. [52]). We report below the main TMM results for the reader's convenience and to make the extension to PTMM easier to follow.

Within a given layer n the zeroth-order electric and magnetic field can be expressed as a multiplication of a 2×2 matrix and a vector containing the amplitudes of the right $f_n^{[0]>}$ and left $f_n^{[0]<}$ propagating waves:

$$\begin{bmatrix} E_n^{[0]}[\omega, z] \\ H_n^{[0]}[\omega, z] \end{bmatrix} = \bar{\bar{a}}_n[\omega, z] \begin{bmatrix} f_n^{[0]>}[\omega] \\ f_n^{[0]<}[\omega] \end{bmatrix}, \qquad (B1)$$

where

$$\bar{\bar{a}}_n[\omega, z] = \begin{bmatrix} e^{i\omega\sqrt{\epsilon_n\mu_n}z} & e^{-i\omega\sqrt{\epsilon_n\mu_n}z} \\ -\sqrt{\frac{\epsilon_n}{\mu_n}}e^{i\omega\sqrt{\epsilon_n\mu_n}z} & \sqrt{\frac{\epsilon_n}{\mu_n}}e^{-i\omega\sqrt{\epsilon_n\mu_n}z} \end{bmatrix}. \qquad (B2)$$

By requiring appropriate continuity equations for the fields at the interfaces between layers, one finds that the field amplitudes at the two air layers to the left and the right of the sample are linked by

$$\begin{bmatrix} f_{N+1}^{[0]>} \\ f_{N+1}^{[0]<} \end{bmatrix} = \bar{\bar{T}}_{[0,N+1]} \begin{bmatrix} f_0^{[0]>} \\ f_0^{[0]<} \end{bmatrix}, \qquad (B3)$$

where $\bar{\bar{T}}_{[0,N+1]}$ is the transfer matrix given by

$$\bar{\bar{T}}_{[0,N+1]} = \bar{\bar{a}}_{N+1}^{-1}[0] \left(\prod_{j=N}^{1} \bar{\bar{a}}_j[d_j]\bar{\bar{a}}_j^{-1}[0] \right) \bar{\bar{a}}_0[0]. \qquad (B4)$$

Furthermore, when contemplating the transfer matrix between any two layers (indexed as n and m, with $n < m$) within the system, it can be formulated in a more general manner:

$$\bar{\bar{T}}_{[n,m]} = \bar{\bar{a}}_m^{-1}[0] \left(\prod_{j=m-1}^{n+1} \bar{\bar{a}}_j[d_j]\bar{\bar{a}}_j^{-1}[0] \right) \bar{\bar{a}}_n[d_n]. \qquad (B5)$$

By solving the set of linear equations presented in Eq. (B3) and utilizing the field expressions from Eq. (B1) we can compute the zeroth-order $E_n^{[0]}$ and $H_n^{[0]}$ fields within any layer.

2. First-order propagation

The set of equations at the first order, as given in Eqs. (A8), cannot be solved through the conventional TMM. These equa-

TABLE II. The theoretical expression and the experimental labeling.

Equation terms	Theoretical labels	Experimental labels
$f_0^{[0]>} * t_a$	$E_{N+1}^{[0]}$	$E_{\text{trans}}^{\text{off}}$
$J_{\text{emit}}^{>} - t_b J_{\text{emit}}^{<}$	–	E_{emit}
$J_{\text{perb}}^{>} - t_b J_{\text{perb}}^{<}$	$E_{N+1}^{[1]}$	$E_{\text{trans}}^{\text{on}} - E_{\text{trans}}^{\text{off}} = \Delta E$

tions are nonhomogeneous and incorporate a source term that depends on $E_n^{[0]}$ and $H_n^{[0]}$. To address Eqs. (A8), we initiate by establishing a general solution to the Maxwell-Drude system with a source term, akin to the approach undertaken in Ref. [53].

The solution can be formulated by combining the general solution related to the homogeneous system with a particular solution. The general solution of the corresponding homogeneous system is achieved by

$$\partial_z E^{[1]}[z, \omega] = -i\omega\mu[\omega]H^{[1]}[z, \omega],$$
$$\partial_z H^{[1]}[z, \omega] = -i\omega\epsilon_T[\omega]E^{[1]}[z, \omega]. \qquad (B6)$$

This can be readily constructed using the standard TMM. We look for a particular solution in the form

$$E^{[1]}[z, t] = E e^{i(k_l z - \omega t)}, \qquad (B7)$$

$$H^{[1]}[z, t] = H e^{i(k_l z - \omega t)}. \qquad (B8)$$

We substitute the above in Eqs. (A8) and obtain the amplitudes of the fields for the particular solution,

$$k_l E = \mu\omega H, \qquad (B9)$$

$$ik_l H = i\epsilon\omega E + \mathcal{J}[k_l, \omega]. \qquad (B10)$$

The particular solution reads

$$\bar{F}[\omega, z] = \begin{bmatrix} E[\omega, z] \\ H[\omega, z] \end{bmatrix} = \mathcal{J}[k_l, \omega]\bar{b}[\omega, k_l, z], \qquad (B11)$$

with

$$\bar{b}[\omega, k, z] = \frac{i e^{ikz}}{\epsilon\mu\omega^2 - k^2} \begin{bmatrix} \omega\mu \\ k \end{bmatrix}. \qquad (B12)$$

With this approach, the first-order correction to the fields within a given layer n is

$$\begin{bmatrix} E_n^{[1]}[\omega, z] \\ H_n^{[1]}[\omega, z] \end{bmatrix} = \bar{\bar{a}}_n[\omega, z]\bar{f}_n[\omega] + \sum_l \mathcal{J}_n[k_l, \omega]\bar{b}[\omega, k_l, z]. \qquad (B13)$$

Without loss of generality, we can assume that only the layer M has time-dependent properties. The general case can be constructed as the summation of first-order corrections due to all the layers that present time-dependent properties. Using the expression in Eq. (B13), the field continuity conditions at all the layers' interfaces can be written. We obtain that the wave intensities in any two layers $n < M$ and $m > M$ are linked by the expression (here the M labeled layer is

TABLE III. Summary of initial inputs.

	Inputs	Physical meaning
Geometry	d_n	Thickness of each layer
	$\gamma^{[0]}$ and $n^{[0]}$	Equilibrium Drude parameters for each layer (layer index suppressed)
Equilibrium material properties	$\epsilon_B(\omega)$	Remaining contribution to the equilibrium dielectric response of the material for each layer (layer index suppressed)
Modification of material properties	$\gamma^{[1]}(t,z)$ and $n^{[1]}(t,z)$	Time- and position-dependent variations of the Drude parameters (layer index suppressed). These are the consequence of the optical laser pump, electron thermalization, carrier recombination, cooling through phonons and/or heat transfer to the substrate, etc. We do not address these dynamics in this work, and we suppose that the induced changes in the Drude parameters are known by other means.
	$f_0^{[0]>}$	We assume that the THz-probe pulse impinges on the sample from the left. Therefore $f[0]>$ represents the incoming THz pulse E-field profile, which is supposed known.
THz probe	$f_{N+1}^{[0]<}, f_0^{[1]>}, f_{N+1}^{[1]<}$	These are all 0.

considered as the excited layer)

$$\begin{bmatrix} f_m^{[1]>} \\ f_m^{[1]<} \end{bmatrix} = \bar{\bar{T}}_{[n,m]} \begin{bmatrix} f_n^{[1]>} \\ f_n^{[1]<} \end{bmatrix} + \sum_l \mathcal{J}[k_l, \omega]\, \bar{\bar{T}}_{[M,m]}$$
$$\times \left(\bar{a}_N^{-1}[d_N]\bar{b}[\omega, k_l, d_N] - \bar{a}_N^{-1}[0]\bar{b}[\omega, k_l, 0] \right),$$

(B14)

where $\bar{\bar{T}}_{[M,m]}$ has an expression similar to Eq. (B5) by replacing all n by M. Finally, considering the two semi-infinite air layers, Eq. (B14) can be recast as

$$\begin{bmatrix} f_{N+1}^{[1]>} \\ f_{N+1}^{[1]<} \end{bmatrix} = \bar{\bar{T}}_{[0,N+1]} \begin{bmatrix} f_0^{[1]>} \\ f_0^{[1]<} \end{bmatrix} + \begin{bmatrix} J_M^> \\ J_M^< \end{bmatrix}.$$

(B15)

The above Eq. (B15) is a pair of linear, frequency-dependent equations where $J_M^<$ and $J_M^<$ can be considered as the generated left- and right-propagating fields in the excited layer. For any fixed source term and for any given incoming field, Eq. (B15) can be used to calculate the transmitted and reflected waves in any layer. When accounting for both the emission source (THz emission from spintronic THz emitter) and the correction source (THz transmission change from OPTP experiments) concurrently, the comprehensive expression becomes

$$\begin{bmatrix} f_{N+1}^{[1]>} \\ f_{N+1}^{[1]<} \end{bmatrix} = \bar{\bar{T}}_{[0,N+1]} \begin{bmatrix} f_0^{[1]>} \\ f_0^{[1]<} \end{bmatrix} + \begin{bmatrix} J_{\text{emit}}^> \\ J_{\text{emit}}^< \end{bmatrix} + \begin{bmatrix} J_{\text{perb}}^> \\ J_{\text{perb}}^< \end{bmatrix}.$$

(B16)

Considering only the transmitted wave at the detector side, the above equation can written in a more simplified form as shown in the main text,

$$f_{N+1}^> = f_0^{[0]>} t_a + (J_{\text{emit}}^> - t_b J_{\text{emit}}^<) + (J_{\text{pert.}}^> - t_b J_{\text{pert.}}^<),$$ (B17)

where

$$t_a = \frac{\bar{\bar{T}}_{[0,N+1],11}\bar{\bar{T}}_{[0,N+1],22} - \bar{\bar{T}}_{[0,N+1],12}\bar{\bar{T}}_{[0,N+1],21}}{\bar{\bar{T}}_{[0,N+1],22}},$$ (B18)

$$t_b = \frac{\bar{\bar{T}}_{[0,N+1],12}}{\bar{\bar{T}}_{[0,N+1],22}},$$ (B19)

with the further subscriptions of $\bar{\bar{T}}_{[0,N+1]}$ referring to the matrix elements.

3. Reflection and transmission

We choose $f_0^{[0]>}(\omega)$ to be the incoming THz probe (from the left) and set $f_{N+1}^{[0]<}(\omega)$ to 0 since no wave is incident from the right. Solving Eq. (B3) for $f_{N+1}^{[0]>}$ and $f_0^{[0]<}$ provides the shape of the zeroth order transmitted and the reflected waves, respectively [52].

Similarly, to solve Eq. (B15) we set $f_0^{[1]>}$ and $f_{N+1}^{[1]<}$ to 0: the optical pump induces no change in the incoming THz probe and also no radiation is coming from the right. We can solve Eq. (B15) for $f_{N+1}^{[1]>}$ and $f_0^{[1]<}$ and obtain the first-order correction to transmitted and reflected waves, respectively. In particular, the correction to the transmission is

$$f_{N+1}^{[1]>} = J_M^> - \frac{\bar{\bar{T}}_{[0,N+1],12}}{\bar{\bar{T}}_{[0,N+1],22}} J_M^<,$$ (B20)

where the further subscriptions of $\bar{\bar{T}}_{[0,N+1]}$ refer to the matrix elements.

Finally, the zeroth-order and first-order electric fields can be calculated as

$$E_{N+1}^{[0]} = f_{N+1}^{[0]>} * \bar{a}_{N+1,11}[\omega, 0],$$ (B21)

$$E_{N+1}^{[1]} = f_{N+1}^{[1]>} * \bar{a}_{N+1,11}[\omega, 0],$$ (B22)

where the further index for $\bar{\bar{a}}$ is the element of the matrix.

A more detailed summary of the relationships between the equation, the theoretical labels, and the experiment labels can be seen in Table II.

APPENDIX C: INPUTS OF PTMM

A summary of the inputs of the calculation of the PTMM is listed in Table III, below.

[1] T. Kampfrath, M. Battiato, P. Maldonado, G. Eilers, J. Nötzold, S. Mährlein, V. Zbarsky, F. Freimuth, Y. Mokrousov, S. Blügel *et al.*, Terahertz spin current pulses controlled by magnetic heterostructures, Nat. Nanotechnol. **8**, 256 (2013).

[2] T. Seifert, S. Jaiswal, U. Martens, J. Hannegan, L. Braun, P. Maldonado, F. Freimuth, A. Kronenberg, J. Henrizi, I. Radu, E. Beaurepaire, Y. Mokrousov, P. M. Oppeneer, M. Jourdan, G. Jakob, D. Turchinovich, L. M. Hayden, M. Wolf, M. Münzenberg, M. Kläui *et al.*, Efficient metallic spintronic emitters of ultrabroadband terahertz radiation, Nat. Photonics **10**, 483 (2016).

[3] M. Battiato, K. Carva, and P. M. Oppeneer, Superdiffusive spin transport as a mechanism of ultrafast demagnetization, Phys. Rev. Lett. **105**, 027203 (2010).

[4] M. Battiato, K. Carva, and P. M. Oppeneer, Theory of laser-induced ultrafast superdiffusive spin transport in layered heterostructures, Phys. Rev. B **86**, 024404 (2012).

[5] Y. Yang, S. Dal Forno, and M. Battiato, Modeling spintronic terahertz emitters as a function of spin generation and diffusion geometry, Phys. Rev. B **107**, 144407 (2023).

[6] J. Liu, K. Lee, Y. Yang, Z. Li, R. Sharma, L. Xi, T. Salim, C. Boothroyd, Y. M. Lam, H. Yang, M. Battiato, and E. E. M. Chia, Spintronic terahertz emitters in silicon-based heterostructures, Phys. Rev. Appl. **18**, 034056 (2022).

[7] P. Agarwal, Y. Yang, R. Medwal, H. Asada, Y. Fukuma, M. Battiato, and R. Singh, Secondary spin current driven efficient THz spintronic emitters, Adv. Opt. Mater. **11**, 2301027 (2023).

[8] P. Agarwal, Y. Yang, J. Lourembam, R. Medwal, M. Battiato, and R. Singh, Terahertz spintronic magnetometer (TSM), Appl. Phys. Lett. **120**, 161104 (2022).

[9] P. Agarwal, R. Medwal, K. Dongol, J. R. Mohan, Y. Yang, H. Asada, Y. Fukuma, and R. Singh, Interfacial spintronic THz emission, arXiv:2308.06224.

[10] X. Wang, L. Cheng, D. Zhu, Y. Wu, M. Chen, Y. Wang, D. Zhao, C. B. Boothroyd, Y. M. Lam, J.-X. Zhu *et al.*, Ultrafast spin-to-charge conversion at the surface of topological insulator thin films, Adv. Mater. **30**, 1802356 (2018).

[11] T. J. Huisman and T. Rasing, THz emission spectroscopy for THz spintronics, J. Phys. Soc. Jpn. **86**, 011009 (2017).

[12] R. Ulbricht, E. Hendry, J. Shan, T. F. Heinz, and M. Bonn, Carrier dynamics in semiconductors studied with time-resolved terahertz spectroscopy, Rev. Mod. Phys. **83**, 543 (2011).

[13] P. A. George, J. Strait, J. Dawlaty, S. Shivaraman, M. Chandrashekhar, F. Rana, and M. G. Spencer, Ultrafast optical-pump terahertz-probe spectroscopy of the carrier relaxation and recombination dynamics in epitaxial graphene, Nano Lett. **8**, 4248 (2008).

[14] J. H. Strait, H. Wang, S. Shivaraman, V. Shields, M. Spencer, and F. Rana, Very slow cooling dynamics of photoexcited carriers in graphene observed by optical-pump terahertz-probe spectroscopy, Nano Lett. **11**, 4902 (2011).

[15] J. Afalla, K. C. Gonzales, E. A. Prieto, G. Catindig, J. D. Vasquez, H. A. Husay, M. A. Tumanguil-Quitoras, J. Muldera, H. Kitahara, A. Somintac *et al.*, Photoconductivity, carrier lifetime and mobility evaluation of GaAs films on Si (100) using optical pump terahertz probe measurements, Semicond. Sci. Technol. **34**, 035031 (2019).

[16] A. Gorodetsky, N. Bazieva, and E. U. Rafailov, Pump dependent carrier lifetimes in InAs/GaAs quantum dot photoconductive terahertz antenna structures, J. Appl. Phys. **125**, 151606 (2019).

[17] N. T. P. Hartono, S. Sun, M. C. Gélvez-Rueda, P. J. Pierone, M. P. Erodici, J. Yoo, F. Wei, M. Bawendi, F. C. Grozema, M.-j. Sher *et al.*, The effect of structural dimensionality on carrier mobility in lead-halide perovskites, J. Mater. Chem. A **7**, 23949 (2019).

[18] P. Krauspe, D. Tsokkou, M. Causa, E. Buchaca-Domingo, Z. Fei, M. Heeney, N. Stingelin, N. Banerji, Terahertz short-range mobilities in neat and intermixed regions of polymer: Fullerene blends with controlled phase morphology, J. Mater. Chem. A **6**, 22301 (2018).

[19] L. Zhang, Z. Chen, R. Zhang, Y. Tan, T. Wu, M. Shalaby, R. Xie, and J. Xu, Direct observation of charge injection of graphene in the graphene/WSe2 heterostructure by optical-pump terahertz-probe spectroscopy, ACS Appl. Mater. Interfaces **11**, 47501 (2019).

[20] K. Mithun, S. Kar, A. Kumar, D. Muthu, N. Ravishankar, and A. Sood, Dirac surface plasmons in photoexcited bismuth telluride nanowires: Optical pump–terahertz probe spectroscopy, Nanoscale **13**, 8283 (2021).

[21] S. Rao, G. Kumar, A. K. Azad, and D. R. Chowdhury, Ultrafast relaxation of charge carriers induced switching in terahertz metamaterials, J Infrared Millim. Terahertz Waves **39**, 1211 (2018).

[22] J. Lu and H. Liu, A critical review on the carrier dynamics in 2D layered materials investigated using THz spectroscopy, Opt. Commun. **406**, 24 (2018).

[23] G. Li, K. Kushnir, Y. Dong, S. Chertopalov, A. M. Rao, V. N. Mochalin, R. Podila, and L. V. Titova, Equilibrium and non-equilibrium free carrier dynamics in 2D $Ti_3C_2T_x$ MXenes: THz spectroscopy study, 2D Mater. **5**, 035043 (2018).

[24] C. La-o-vorakiat, L. Cheng, T. Salim, R. A. Marcus, M.-E. Michel-Beyerle, Y. M. Lam, and E. E. M. Chia, Phonon features in terahertz photoconductivity spectra due to data analysis artifact: A case study on organometallic halide perovskites, Appl. Phys. Lett. **110**, 123901 (2017).

[25] S. Kar, Y. Su, R. R. Nair, and A. K. Sood, Probing photoexcited carriers in a few-layer MoS2 laminate by time-resolved optical pump-terahertz probe spectroscopy, ACS Nano **9**, 12004 (2015).

[26] S. Kar, D. R. Mohapatra, E. Freysz, and A. K. Sood, Tuning photoinduced terahertz conductivity in monolayer graphene:

Optical-pump terahertz-probe spectroscopy, Phys. Rev. B **90**, 165420 (2014).

[27] A. Tomadin, S. M. Hornett, H. I. Wang, E. M. Alexeev, A. Candini, C. Coletti, D. Turchinovich, M. Kläui, M. Bonn, F. H. Koppens *et al.*, The ultrafast dynamics and conductivity of photoexcited graphene at different Fermi energies, Sci. Adv. **4**, eaar5313 (2018).

[28] S. Ruan, X. Lin, H. Chen, B. Song, Y. Dai, X. Yan, Z. Jin, G. Ma, and J. Yao, Terahertz probe of nonequilibrium carrier dynamics and ultrafast photocurrents in the topological insulator Sb2Te3, Appl. Phys. Lett. **118**, 011102 (2021).

[29] B. G. Alberding, G. P. Kushto, P. A. Lane, and E. J. Heilweil, Reduced photoconductivity observed by time-resolved terahertz spectroscopy in metal nanofilms with and without adhesion layers, Appl. Phys. Lett. **108**, 223104 (2016).

[30] T. Kürner and S. Priebe, Towards THz communications—Status in research, standardization and regulation, J. Infrared, Millimeter, Terahertz Waves **35**, 53 (2014).

[31] S. Koenig, D. Lopez-Diaz, J. Antes, F. Boes, R. Henneberger, A. Leuther, A. Tessmann, R. Schmogrow, D. Hillerkuss, R. Palmer *et al.*, Wireless sub-THz communication system with high data rate, Nat. Photonics **7**, 977 (2013).

[32] L. Bassman Oftelie, K. Liu, A. Krishnamoorthy, T. Linker, Y. Geng, D. Shebib, S. Fukushima, F. Shimojo, R. K. Kalia, A. Nakano, and P. Vashishta, Towards simulation of the dynamics of materials on quantum computers, Phys. Rev. B **101**, 184305 (2020).

[33] N. Takanashi, A. Inoue, T. Kashiwazaki, T. Kazama, K. Enbutsu, R. Kasahara, T. Umeki, and A. Furusawa, All-optical phase-sensitive detection for ultra-fast quantum computation, Opt. Express **28**, 34916 (2020).

[34] E. Beaurepaire, J.-C. Merle, A. Daunois, and J.-Y. Bigot, Ultrafast spin dynamics in ferromagnetic nickel, Phys. Rev. Lett. **76**, 4250 (1996).

[35] A. Eschenlohr, M. Battiato, P. Maldonado, N. Pontius, T. Kachel, K. Holldack, R. Mitzner, A. Föhlisch, P. M. Oppeneer, and C. Stamm, Ultrafast spin transport as key to femtosecond demagnetization, Nat. Mater. **12**, 332 (2013).

[36] E. Carpene, E. Mancini, C. Dallera, M. Brenna, E. Puppin, and S. De Silvestri, Dynamics of electron-magnon interaction and ultrafast demagnetization in thin iron films, Phys. Rev. B **78**, 174422 (2008).

[37] T. Kampfrath, R. G. Ulbrich, F. Leuenberger, M. Münzenberg, B. Sass, and W. Felsch, Ultrafast magneto-optical response of iron thin films, Phys. Rev. B **65**, 104429 (2002).

[38] W. S. Fann, R. Storz, H. W. K. Tom, and J. Bokor, Electron thermalization in gold, Phys. Rev. B **46**, 13592 (1992).

[39] C.-K. Sun, F. Vallée, L. H. Acioli, E. P. Ippen, and J. G. Fujimoto, Femtosecond-tunable measurement of electron thermalization in gold, Phys. Rev. B **50**, 15337 (1994).

[40] C. Suárez, W. E. Bron, and T. Juhasz, Dynamics and transport of electronic carriers in thin gold films, Phys. Rev. Lett. **75**, 4536 (1995).

[41] H. Němec, F. Kadlec, C. Kadlec, P. Kužel, and P. Jungwirth, Ultrafast far-infrared dynamics probed by terahertz pulses: A frequency-domain approach. II. Applications, J. Chem. Phys. **122**, 104504 (2005).

[42] H. Němec, F. Kadlec, S. Surendran, P. Kužel, and P. Jungwirth, Ultrafast far-infrared dynamics probed by terahertz pulses: A frequency domain approach. I. Model systems, J. Chem. Phys. **122**, 104503 (2005).

[43] H. Němec, F. Kadlec, and P. Kužel, Methodology of an optical pump-terahertz probe experiment: An analytical frequency-domain approach, J. Chem. Phys. **117**, 8454 (2002).

[44] P. Kužel, F. Kadlec, and H. Němec, Propagation of terahertz pulses in photoexcited media: Analytical theory for layered systems, J. Chem. Phys. **127**, 024506 (2007).

[45] H.-K. Nienhuys and V. Sundström, Intrinsic complications in the analysis of optical-pump, terahertz probe experiments, Phys. Rev. B **71**, 235110 (2005).

[46] J. M. Schins, E. Hendry, M. Bonn, and H. Muller, Retrieving the susceptibility from time-resolved terahertz experiments, J. Chem. Phys. **127**, 094308 (2007).

[47] J. M. Schins, Interpretation of ultrafast pump-probe terahertz experiments in the time domain: How to exploit two-dimensional correlations, Phys. Rev. B **83**, 205111 (2011).

[48] L. Fekete, F. Kadlec, H. Němec, and P. Kužel, Fast one-dimensional photonic crystal modulators for the terahertz range, Opt. Express **15**, 8898 (2007).

[49] M. C. Beard, G. M. Turner, and C. A. Schmuttenmaer, Transient photoconductivity in GaAs as measured by time-resolved terahertz spectroscopy, Phys. Rev. B **62**, 15764 (2000).

[50] M. C. Beard, G. M. Turner, and C. A. Schmuttenmaer, Sub-picosecond carrier dynamics in low-temperature grown GaAs as measured by time-resolved terahertz spectroscopy, J. Appl. Phys. **90**, 5915 (2001).

[51] M. C. Beard and C. A. Schmuttenmaer, Using the finite-difference time-domain pulse propagation method to simulate time-resolved THz experiments, J. Chem. Phys. **114**, 2903 (2001).

[52] Y. Yang, S. Dal Forno, and M. Battiato, Removal of spectral distortion due to echo for ultrashort THz Pulses propagating through multilayer structures with thick substrate, J. Infrared, Millimeter, Terahertz Waves **42**, 1142 (2021).

[53] Y. Yang, S. Dal Forno, and M. Battiato, Transfer-matrix description of heterostructured spintronics terahertz emitters, Phys. Rev. B **104**, 155437 (2021).

[54] J. B. Baxter and C. A. Schmuttenmaer, Time-resolved terahertz spectroscopy and terahertz emission spectroscopy, *Terahertz Spectroscopy: Principles and Applications* (CRC Press, Boca Raton, FL, 2008), p. 73.

[55] C. L. Davies, J. B. Patel, C. Q. Xia, L. M. Herz, and M. B. Johnston, Temperature-dependent refractive index of quartz at terahertz frequencies, J. Infrared, Millimeter, Terahertz Waves **39**, 1236 (2018).

[56] M. Naftaly and R. E. Miles, Terahertz time-domain spectroscopy of silicate glasses and the relationship to material properties, J. Appl. Phys. **102**, 043517 (2007).

[57] M. A. Ordal, R. J. Bell, R. W. Alexander, L. L. Long, and M. R. Querry, Optical properties of fourteen metals in the infrared and far infrared: Al, Co, Cu, Au, Fe, Pb, Mo, Ni, Pd, Pt, Ag, Ti, V, and W, Appl. Opt. **24**, 4493 (1985).